NJC

ROYAL SOCIETY OF CHEMISTRY

PAPER

View Article Online
View Journal

Cite this: DOI: 10.1039/d3nj02294c

Zirconium-doped BiOCl for enhanced visible light-induced photocatalytic degradation of RhB dye and photoelectrochemical studies

Asyiqin Zulkiflee,[a] Mohammad Mansoob Khan, *[a] Mohd Yusuf Khan,[b] Abuzar Khan, [b] Aniz Chennampilly Ummer [c] and Mohammad Hilni Harunsani [a]

Photocatalytic degradation is considered to be a promising approach for treating water contamination caused by industrialization. Hence, an eco-friendly photocatalyst with high efficiency is needed. Bismuth oxychloride (BiOCl) and Zr-doped BiOCl (ZBCl) with enhanced visible light-induced photocatalytic activities were prepared through a simple co-precipitation method at ambient conditions. The synthesized materials were characterized using XRD, FT-IR, Raman, UV-Vis DRS, PL, TEM, HRTEM, and BET analysis. Photocatalytic studies showed that ZBCl possesses higher photocatalytic activity for the degradation of rhodamine B under visible light irradiation in comparison to BiOCl. Among the synthesized materials, the 1% ZBCl exhibited the highest photocatalytic efficiency. The 1% ZBCl was able to degrade 97.7% of RhB dye within 60 min. Additionally, the linear sweep voltammetry (LSV) and electrochemical impedance spectroscopy (EIS) studies showed enhanced response under visible light irradiation in comparison to dark conditions which is caused by a decrease in electron transfer resistance and an increase in photocurrent. This research suggests that ZBCl can be used successfully as a photocatalyst and as a photoelectrode material due to its enhanced photocatalytic and photoelectrochemical response.

Received 18th May 2023,
Accepted 10th August 2023

DOI: 10.1039/d3nj02294c

rsc.li/njc

1. Introduction

Environmental contamination is a major challenge as a result of industrialization.[1–3] Contaminant degrading strategies that are both effective and environmentally friendly are sorely needed.[4,5] Synthetic organic dyes such as rhodamine B (RhB) are commonly utilized in a variety of industries, including textiles, food, beauty products, and pharmaceutical industries.[6] RhB effluent is harmful and can cause severe health issues such as inflammation of the respiratory tract, eyes, and skin.[7] In addition, the discharge of dyes from several industries endangers the ecosystem by interfering with phytoplankton and mammals *via* the food chain, which has sparked a lot of research interest in organic wastewater treatment.[8] Numerous approaches for removing these hazardous dyes have been documented.[8] Dye pollutants have been removed using adsorption, coagulation, ion exchange membrane filtration, biological, and chemical treatment techniques.[9] Several approaches mentioned above end up in incomplete dye degradation, resulting in subsequent hazardous intermediates.[10] Researchers have paid close consideration to semiconductor photocatalytic technology because of its vast application potential in resolving energy demand and pollution.[11–14] Under solar irradiation, photocatalysts such as titanium dioxide (TiO_2) have been proven to be efficient by degrading organic water pollutants.[15,16] Moreover, TiO_2 is also considered as a promising material for photoelectrochemical (PEC) applications because of its great redox capability, highly resistance to photo-corrosion, high durability, natural abundance, non-toxic, and inexpensive.[17–19] Nonetheless, applicability of TiO_2 was hindered due to the low separation efficiency of photo-generated electrons and holes and wide band gap. As a result, it was proposed that high-efficiency photocatalysts be designed to replace TiO_2.[20]

Due to its unique layered structure, bismuth oxychloride (BiOCl) has received a considerable amount of attention. It is non-toxic, chemically stable, and has high resistance against photo-corrosion.[21] Moreover, its layers of $[Cl]^-$ alternate with

[a] *Chemical Sciences, Faculty of Science, Universiti Brunei Darussalam, Jalan Tungku Link, Gadong, BE 1410, Brunei Darussalam. E-mail: mmansoobkhan@yahoo.com, mansoob.khan@ubd.edu.bn*

[b] *Interdisciplinary Research Center for Hydrogen and Energy Storage, King Fahd University of Petroleum & Minerals (KFUPM), Dhahran, 31261, Saudi Arabia*

[c] *Interdisciplinary Research Center for Refining and Advanced Chemicals (IRC-CRAC), King Fahd University of Petroleum & Minerals (KFUPM), Dhahran, 31261, Saudi Arabia*

layers of $[Bi_2O_2]^{2+}$ in this compound stacked structure.[22,23] The photocatalytic efficiency of BiOCl is improved by the minimization of charge recombination which is associated with the electrostatic force between the $[Cl]^-$ and $[Bi_2O_2]^{2+}$ layers.[23–25] BiOCl has an estimated band gap within the range of 3.02 to 3.50 eV.[26,27] Despite the fact that BiOCl is a broad band semiconductor, it can photosensitize and decompose organic dyes when exposed to visible light.[28,29] This can be obtained through the transport of electrons from excited dye molecules into the conduction band of a semiconductor after the light-induced excitation of dye molecules.[28,30] In addition, doping this material with metal and non-metal elements, as well as generating oxygen vacancies, are some of the methods used for improving its photocatalytic performance.[31–35] Among the numerous strategies, doping BiOCl with transition metal ions has been found to be effective in forming energy states in the forbidden energy gap of BiOCl, minimizing the band gap energy of the material, increasing the number of electron–hole pairs produced, and thus, boosting photocatalytic efficiency under light irradiation.[36,37] For instance, Xu *et al.* prepared flower like La-doped BiOCl and it showed higher photocatalytic activity compared to BiOCl.[38] Moreover, Wang *et al.* mentioned that Co-doped BiOCl degraded 95% of Bisphenol A whilst BiOCl degraded 20% in 120 min.[39] Pare *et al.* degraded malachite green with Mn–BiOCl under visible light irradiation, and achieved a removal efficiency of 98% within 120 min.[40]

Based on these findings, it is believed that doping BiOCl with zirconium (Zr) could be a promising strategy to improve the photocatalytic performance under visible light irradiation. To the best of the authors' knowledge, the synthesis of Zr-doped BiOCl has not been reported yet. In this study, BiOCl and Zr-doped BiOCl was synthesized using a simple co-precipitation method at ambient conditions. The phase, structures, morphologies, and optical characteristics of the fabricated materials were studied in depth using several techniques, including Powder X-ray diffraction (XRD), Fourier transform infrared spectroscopy (FT-IR), Raman spectroscopy, Transmission electron microscope (TEM), Brunauer Emmett–Teller (BET), UV-visible diffuse reflectance spectroscopy (UV-Vis DRS), and Photoluminescence spectroscopy (PL). The photocatalytic activity of the BiOCl and Zr-doped BiOCl was investigated by degrading RhB dye in the presence of visible light. The photoelectrochemical studies such as linear sweep voltammetry (LSV) and electrochemical impedance spectroscopy (EIS) were carried out in the dark and under visible light irradiation to further investigate photoelectrochemical activity of the BiOCl and Zr-doped BiOCl induced by visible light.

2. Experimental method

2.1. Materials

Bismuth nitrate pentahydrate ($Bi(NO_3)_3{\cdot}5H_2O$, 97%) were obtained from VWR, USA. Potassium chloride (KCl) and zirconium nitrate ($Zr(NO_3)_4$) were obtained from BDH, UK. Ethylene glycol ($(CH_2OH)_2$, 99.8%) and ethyl cellulose (48.0–49.5%(w/w) ethoxyl basis) were purchased from Sigma Aldrich, Germany. α-terpineol were obtained from Merck, Germany. Ethanol (C_2H_5OH, 95%) was acquired from Daejung Chemicals and Metals Co. Ltd, South Korea. Sodium sulfite anhydrous (Na_2SO_3) were acquired from Fisher Scientific, USA. A fluorine-doped tin oxide (FTO) glass electrode by 2 cm × 1 cm was used as the working electrode. Throughout the experiment, double distilled water was utilized, which was purified using Aquatron, England.

2.2. Instrumentation

The crystal phase structure of the as-prepared materials was carried out using a Rigaku MiniFlex (λ = 1.5406 Å). The samples were recorded at the 2θ value between 20–80° at a scan rate of $2^\circ\ min^{-1}$. FT-IR were performed using Shimadzu IRSpirit and were scanned at wavenumber range between 400–4000 cm^{-1} to analyze the vibrational modes present in the samples. Raman microscope (DXR, Thermo Scientific) was used to determine the chemical species with an excitation wavelength of 255 nm (laser power of 2.5 mW). The morphology and particle size of the materials were obtained *via* TEM (JEOL JEM 2100F). The N_2 adsorption–desorption measurements were performed on ASAP 2020 torsimeter (Micrometrics). The samples were heated to 150 °C with a heating rate of 10 °C min^{-1} and then degassed at 150 °C for 200 min followed by nitrogen adsorption at −196 °C. The specific surface area of the samples was calculated using BET method. The UV-Vis DRS analysis of the powdered BiOCl and Zr-doped BiOCl samples was examined using a Shimadzu UV 2600 double beam spectrophotometer. PL was performed using a Jasco FP-8500ST fluorescence spectrophotometer. The UV-Vis DRS and PL were employed to measure the optical properties of the samples. The photocatalytic processes of the photocatalyst were conducted using a TOPTION V photoreactor equipped with a 300 W Xenon lamp. The photocatalytic degradation of RhB was analyzed using Shimadzu UV-1900 UV-visible spectrophotometer (UV-Vis). The photoelectrochemical studies (EIS and LSV) measurements were recorded using a potentiostat Autolab (MetroHm, Herisau, Switzerland) under dark and visible light irradiation (Simon FL30 LED Floodlight, Jiangsu, China).

2.3. Synthesis of BiOCl

Firstly, 0.80 mmol of $Bi(NO_3)_3{\cdot}5H_2O$ was dissolved in 9.60 mL of ethylene glycol. This solution was stirred at room temperature for 20 min. Next, 0.80 mmol of KCl was suspended in 9.60 mL of double distilled water. After 20 min, the KCl solution was added to the above Bi solution and vigorously stirred for 1 h at room temperature. After that, the white product was collected *via* centrifugation. The product was then washed with water and ethanol three times. After drying at 80 °C, the solid was grounded using an agate mortar and pestle. The final product of fine white powder was obtained.

2.4. Synthesis of Zr-doped BiOCl

In order to synthesize Zr-doped BiOCl, 0.80 mmol of $Bi(NO_3)_3{\cdot}5H_2O$ and a desired amount (0.5%, 1%, and 5%) of $Zr(NO_3)_4$

was suspended in 9.60 mL of double distilled water and magnetically stirred for 20 min. After that, 0.80 mmol of KCl solution was added into the mixture and vigorously stirred for 1 h. The obtained product was collected *via* centrifugation. The product was then washed with water and ethanol three times. After drying at 80 °C, the solids were grounded into fine powders using an agate mortar and pestle. The desired amount of Zr-doped BiOCl prepared was 0.5%, 1%, and 5% and referred to as 0.5% ZBCl, 1% ZBCl and 5% ZBCl.

2.5. Photocatalytic performance of BiOCl and Zr-doped BiOCl

To assess the photocatalytic performance under visible light irradiation, RhB dye was chosen as the target pollutant and 300 W Xe lamp was used as the visible light source. Typically, 20 mg of photocatalyst was suspended in 50 mL of 10 ppm of RhB aqueous solution. To ensure adsorption–desorption equilibrium, the suspension was sonicated for 10 min and stirred in the dark for 30 min before the photocatalytic reaction. After that, the reaction was carried out under visible light irradiation for 1 h. At each interval of 10 min, 3 mL of the suspension was taken and centrifuged to separate the photocatalyst. Subsequently, the photocatalytic degradation efficiency of BiOCl and Zr-doped BiOCl was measured using a UV-Vis spectrophotometer and were scanned between the wavelengths of 200–800 nm.

2.6. Photoelectrochemical studies of BiOCl and Zr-doped BiOCl

For LSV and EIS studies, the working electrodes were prepared with 25 mg of each sample that had been fully dispersed in 500 μL of ethanol and α-terpineol and sonicated for 10 min. The sonicated mixture was followed by the addition of 25 mg of ethyl cellulose as a binder. The mixture was heated at 80 °C and magnetically stirred for 1 h to make a thick paste. The paste was coated on FTO glass electrode using the doctor-blade method. The LSV and EIS measurements were carried out using a potentiostat with a simple three-electrode system, in which BiOCl and ZBCl (coated on FTO glass), Pt sheet, and Ag/AgCl were employed in the system as the working electrode, counter electrode, and reference electrode, respectively. For each electrode, the LSV and EIS experiments of BiOCl and ZBCl were conducted under ambient conditions in the dark and under visible light irradiation in 80 mL of 0.1 M Na_2SO_3 aqueous solution. The LSV and EIS was measured at the potential range of −0.8 to 1.2 V at a scan rate of 50 mV s^{-1} and a frequency range of 100 kHz to 0.1 Hz, respectively.

3. Results and discussion

3.1. Powder XRD analysis

Powder XRD technique was used to determine the phase and crystallinity of the synthesized materials. The XRD patterns of synthesized BiOCl and 0.5%, 1%, and 5% ZBCl samples are shown in Fig. 1. It was observed that the most intense peaks positions were seen at about 2θ = 25.91°, 32.57°, and 33.46°

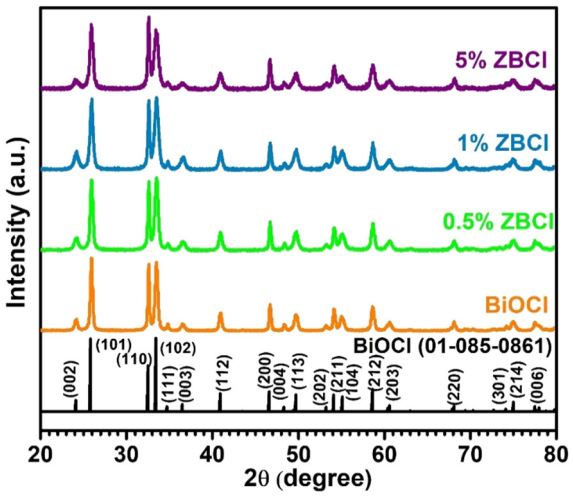

Fig. 1 The XRD patterns of BiOCl, 0.5% ZBCl, 1% ZBCl, and 5% ZBCl.

which corresponds to the (101), (110), and (102) planes of tetragonal phase of BiOCl (JCPDS card no. 01-085-0861), respectively.[41] No other impurity peaks were found in the diffraction pattern which indicates that the samples are pure. Furthermore, the crystallite size of the samples was evaluated from the XRD patterns. Crystallite size of the BiOCl, 0.5% ZBCl, 1% ZBCl, and 5% ZBCl was calculated using Debye–Scherrer equation shown in eqn (1),

$$D = \frac{K\lambda}{\beta \cos\theta} \quad (1)$$

where D is crystallite size, β = FWHM (Full width at half maximum), λ = X-ray wavelength used, θ = Bragg angle, and K = 0.9.

It was found that the crystallite size decreases as the doping increases. However, the doping has little effect on the lattice parameters and the unit cell volume. This result is in agreement with a study reported by Xie *et al.* where Sn-doping has negligible effect on the lattice constants and unit cell volume.[42] This indicates that the doping samples maintain the crystal structure of the undoped samples. In the standard of BiOCl, the peak ratio between the (110) and (102) plane was 0.63. Furthermore, the peak ratio of the as-prepared BiOCl, 0.5% ZBCl, 1% ZBCl, and 5% ZBCl were 0.97, 0.86, 0.91, and 1.10, respectively. Therefore, it can be deduced that the crystal growth along the (110) direction is preferred.[39] The calculated lattice parameters, unit cell volume, and the mean crystallite size of the samples are shown in Table 1.

3.2. FT-IR analysis

The FT-IR spectra of BiOCl, 0.5%, 1%, and 5% of Zr-doped BiOCl are shown in Fig. 2(a). It can be deduced that the absorption band around 526 cm^{-1} belongs to the Bi–O bond.[43] The weak absorption band at 1382 cm^{-1} is assigned to Bi–Cl band. Lastly, the peak at 1622 cm^{-1} is due to the bending vibrations of adsorbed OH species.[41] As seen from Fig. 2(a), no additional peaks were observed. Moreover, the

Table 1 Lattice parameters, unit cell volume, and mean crystallite size of the as-synthesised BiOCl, 0.5% ZBCl, 1% ZBCl, and 5% ZBCl

Samples	Lattice parameters (Å)		Unit cell volume (Å^3)	Mean crystallite size (nm)
	a	*c*		
BiOCl	3.885	7.371	111.26	34.60
0.5% ZBCl	3.885	7.351	110.97	28.57
1% ZBCl	3.886	7.362	111.16	25.09
5% ZBCl	3.887	7.373	111.41	23.10

Bi–O band of BiOCl has a sharp peak and as the Zr content increases, the intensity of this peak also decreases. This indicates that Zr dopant is introduced into the BiOCl lattice.[43] In comparison with Y-doped BiOBr synthesized using ethylene glycol as a solvent, the author explained that the peak at 1394 cm^{-1} belongs to the Bi–Br band which has similar value with Bi–Cl band obtained.[43,44] Tang *et al.* deduced that peak at 1375 cm^{-1} is assigned to Bi–I band in BiOI.[45] Based on these FT-IR results, it can be suggested that Zr is successfully incorporated into the BiOCl lattice which is in agreement with the XRD results.

3.3. Raman spectroscopy

The chemical structures of the synthesized products were analyzed using Raman spectroscopy. From the Raman spectra (Fig. 2(b)), it was observed that three different vibrational peaks are present. This is due to the mobility of halogen atoms on the BiOCl surface that is reflected in the Bi–Cl bands, which are found at three different wavenumbers. The peaks at 143 and 198 cm^{-1} were attributed to Bi–Cl with A_{1g} and E_g stretching mode, respectively. Furthermore, the bands at 393 cm^{-1} are due to the vibrations of Bi–O.[46,47] Although no additional peaks were seen due to doping of Zr, the peak around 198 cm^{-1} of the ZBCl samples shifts to the left. This might be due to the reduction of crystallite size.[48] These similar findings were reported in literature.[48–50] Kim *et al.* studied the Raman spectra of $BiOCl_xI_{1-x}$ and three prominent peaks were observed at 144 cm^{-1}, 200 cm^{-1}, and 390 cm^{-1}.[51] In another study, Xia *et al.* also found similar peaks for Fe–BiOCl around 143.7 cm^{-1} and 198.6 cm^{-1} which is assigned to the A_{1g} and E_g of Bi–Cl stretching mode.[52] This finding further indicates the successful formation of BiOCl and ZBCl and is in accord with the XRD and FT-IR analysis.

3.4. UV-Vis DRS analysis

The optical properties of the BiOCl and ZBCl were measured by means of UV-Vis DRS. The Kubelka–Munk function plots were used to investigate the effect of doping as depicted in Fig. 3(a), including the plot absorbance of all the as-synthesized materials are shown in inset (a). The band gap energy of the prepared samples was calculated using the Kubelka–Munk function as shown in eqn (2):

$$F(R) = \left(\frac{(1-R)^2}{2R} \times hv\right)^{1/2} \quad (2)$$

where R is the measured absolute reflectance of the samples. The band gap energy was calculated from the corresponding plots of $[F(R)hv]^{1/2}$ *versus* hv, as the intercept of the extrapolated linear part of the plot at $[F(R)hv]^{1/2} = 0$, assuming that the absorption coefficient (α) is proportional to the Kubelka–Munk function $F(R)$. From the inset in Fig. 3(a), it was observed that BiOCl exhibits the typical UV light response with absorption edge around 343 nm and the estimated band gap is 3.40 eV.

The estimated band gap of the synthesized materials is summarized in Table 2. It can be suggested that doping with Zr has a minor effect on the narrowing of the band gap. This similar outcome can be found in other studies. For example, Yang *et al.* examined the band gap of BiOCl and Dy-doped BiOCl to be 3.29 and 3.00 eV, respectively.[48] Moreover, Wang *et al.* investigated the band gap of BiOCl and Co-doped BiOCl to be 3.17 and 3.09 eV.[39] This shows that the addition of dopant can have varying influence on the band gap energy of BiOCl.

3.5. PL analysis

In order to study the charge recombination efficiency of the synthesized materials, PL was employed. Fig. 3(b) displays the PL emission spectra of all the samples measured at an excitation wavelength of 255 nm. Both BiOCl and all ZBCl materials

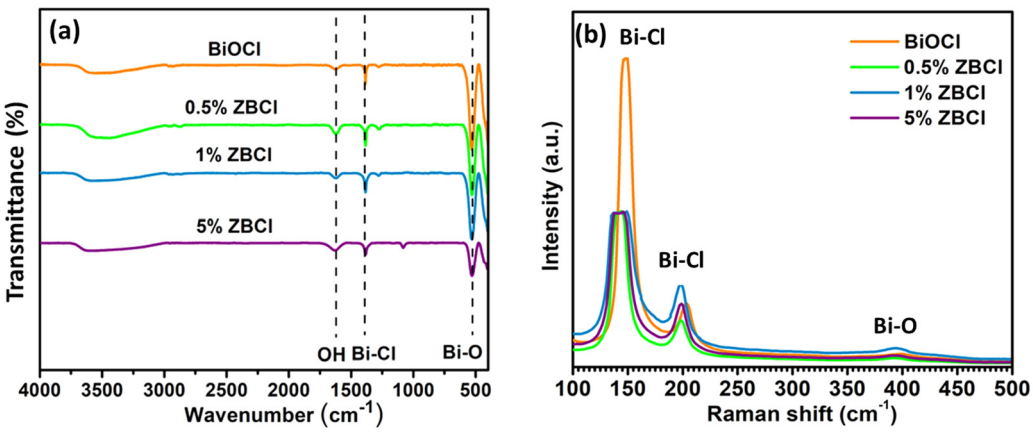

Fig. 2 (a) FTIR and (b) Raman spectra of BiOCl, 0.5% ZBCl, 1% ZBCl, and 5% ZBCl.

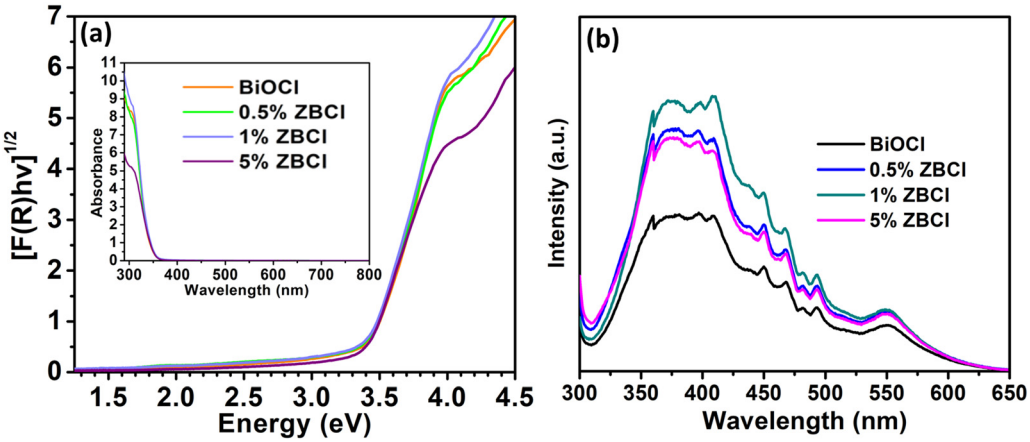

Fig. 3 (a) Tauc plots constructed from Kubelka–Munk transformed diffuse reflectance and (b) PL spectra of BiOCl, 0.5% ZBCl, 1% ZBCl, and 5% ZBCl. Inset in (a) shows the plot of −log reflectance (*i.e.* absorbance) of all the as-synthesized materials.

Table 2 The band gap energies of the as-synthesized materials estimated from Kubelka–Munk function

Samples	Band gap energy (eV)
BiOCl	3.40
0.5% ZBCl	3.35
1% ZBCl	3.31
5% ZBCl	3.34

showed similar curves and no peak shifts were observed. Moreover, the PL intensity increases after the incorporation of the Zr dopant in the BiOCl lattice. This might be due to the presence of surface oxygen vacancies and defect.[53,54] The higher the content of oxygen vacancies, the greater the peak intensity.[53–56] This result suggested that oxygen vacancies could be present in ZBCl and might be one of the factors that enhances the photocatalytic activity.

3.6. TEM analysis

TEM is used to determine the morphology and particle size of the as-prepared BiOCl and ZBCl samples. In Fig. 4, TEM images of (a)–(b) BiOCl and (e)–(f) 1% ZBCl were observed to have irregular nanoplates with size of 80–100 nm. It can also be seen that there were no major changes in the morphology. Furthermore, the thickness of the BiOCl and 1% ZBCl nanoplates were around 17 nm and 12 nm, respectively. Similar thickness was also reported in a morphological study of the Co-doped BiOCl.[39] The high resolution transmission electron microscopy (HRTEM) of BiOCl (Fig. 4(c)) and 1% ZBCl (Fig. 4(g)) shows clear lattice fringes, indicating good crystallinity of the samples. Moreover, the focused area of the HRTEM images of BiOCl (Fig. 4(d)) and 1% ZBCl (Fig. 4(h)) samples shows lattice spacings marked by yellow arrow and lines. The clear lattice fringes were calculated to have lattice spacings of 0.263 nm and 0.322 nm, respectively. The lattice spacing values correlates to the theoretical interplanar spacings of (102) and (002) crystal plane of tetragonal BiOCl.[57] The calculated *d*-spacings of BiOCl

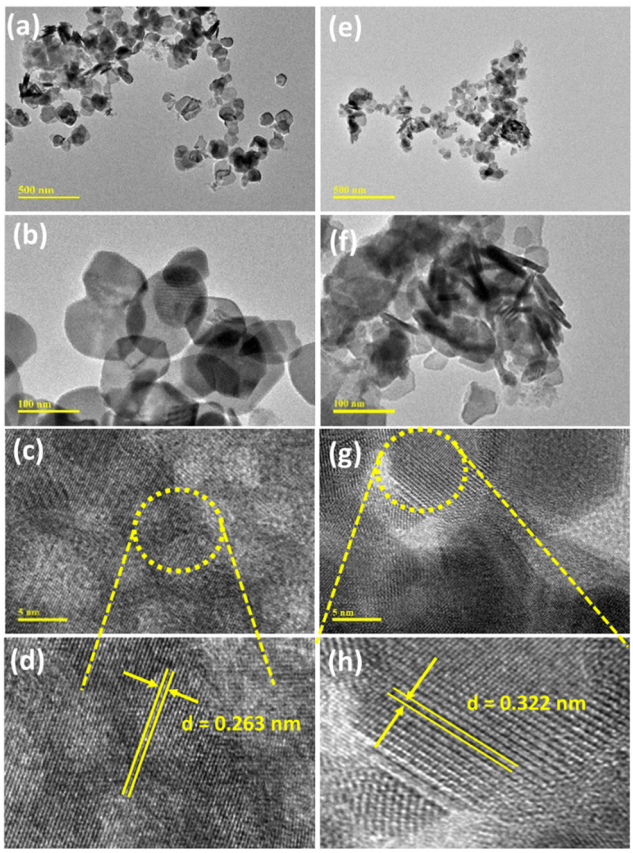

Fig. 4 TEM images of (a)–(b) BiOCl and (e)–(f) 1% ZBCl. The HRTEM images of (c) BiOCl and (g) 1% ZBCl can be shown with its focused area in (d) and (h), respectively.

and Fe-doped BiOCl were in agreement with the tetragonal system of BiOCl. It was found that adding Fe has little effect on the crystal structure, morphology, and particle size.[57] These results are in accordance with the XRD analysis and suggests that Zr doping has a minor effect on the crystal structure, morphology and particle size.

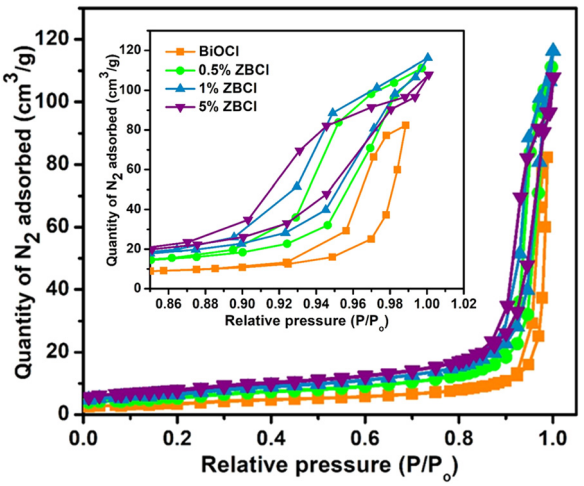

Fig. 5 N_2 adsorption and desorption isotherms of BiOCl, 0.5% ZBCl, 1% ZBCl, and 5% ZBCl. Inset shows the zoom region of P/P_0 between 0.84–1.02.

Table 3 Specific surface area of BiOCl, 0.5% ZBCl, 1% ZBCl, and 5% ZBCl

Samples	BET specific surface area ($m^2\ g^{-1}$)
BiOCl	13.49
0.5% ZBCl	20.87
1% ZBCl	25.36
5% ZBCl	28.89

3.7. BET analysis

The specific surface areas of the as-prepared samples were investigated by BET analysis. The nitrogen adsorption and desorption isotherms of BiOCl, 0.5%, 1%, and 5% ZBCl is shown in Fig. 5. All of the samples display a type-IV isotherm with a type H3 hysteresis loop, confirming the presence of mesopore.[58,59] The specific surface area of BiOCl is 13.49 $m^2\ g^{-1}$. With the increase of Zr content, the value of the specific surface area gradually increased from 13.49 to 28.89 $m^2\ g^{-1}$. The BET specific surface areas of the as-prepared samples are listed in Table 3.

4. Evaluation of photocatalytic efficiency

Using RhB organic dye as the model pollutant, the photocatalytic performance of the fabricated materials was assessed under visible light irradiation within 1 h. In Fig. 6, the results of the photocatalytic degradation of RhB dye using the synthesized materials where (a) the kinetic analysis of RhB photocatalytic degradation, and (b) the percentage photocatalytic degradation rate for each sample are shown. Among the doped samples, it can be deduced that 1% ZBCl was most efficient in degrading RhB dye. The kinetic analysis was investigated for a better comparability of the photocatalytic efficiency of the as-prepared photocatalysts using the pseudo-first-order kinetics model, $-\ln(C/C_0) = kt$ where C_0 and C_t are the concentrations of RhB dye at time 0 and t (min), accordingly and k (min^{-1}) is the pseudo-first-order rate constant. Fig. 6(a) shows the rate constant of the ZBCl samples were higher than BiOCl. The rate constant of BiOCl is 0.0168 min^{-1} and the highest rate constant among the ZBCl samples is for 1%, which is three times higher than that of BiOCl. In addition, the photocatalytic efficiency starts to slow down as the Zr content increases. This indicates that the photocatalytic degradation was not favored by excessive doping. Among the doped BiOCl samples, ZBCl with a concentration of 1% shows the best photocatalytic efficiency. Hence as shown in Fig. 6(b), BiOCl, 0.5%, 1%, and 5% ZBCl was able to degrade 64.3%, 92.7%, 97.7% and 84.9% of the RhB dye, respectively. BiOCl and 1% ZBCl were able to degrade 64.3% and 97.7% of RhB dye within 60 min. This similar photocatalytic performance can be found in other studies. For instance, Mokhtari *et al.* fabricated BiOCl and 1% W-doped BiOCl possessed a band gap of 3.29 and 3.00 eV, correspondingly. Moreover, BiOCl and W-doped BiOCl were able to degrade 8% and 90% in 180 min.[36]

5. Evaluation of photoelectrochemical efficiency

The enhanced visible light photoactivity of ZBCl was further examined by measuring the photocurrent using LSV in the dark

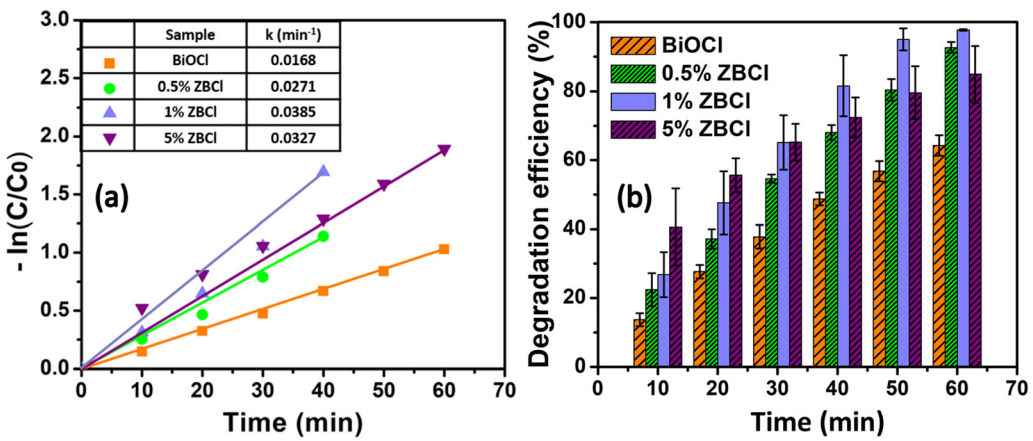

Fig. 6 (a) $-\ln(C/C_0)$, pseudo-first-order kinetics, and (b) degradation efficiency of the synthesized materials using RhB dye under visible light irradiation.

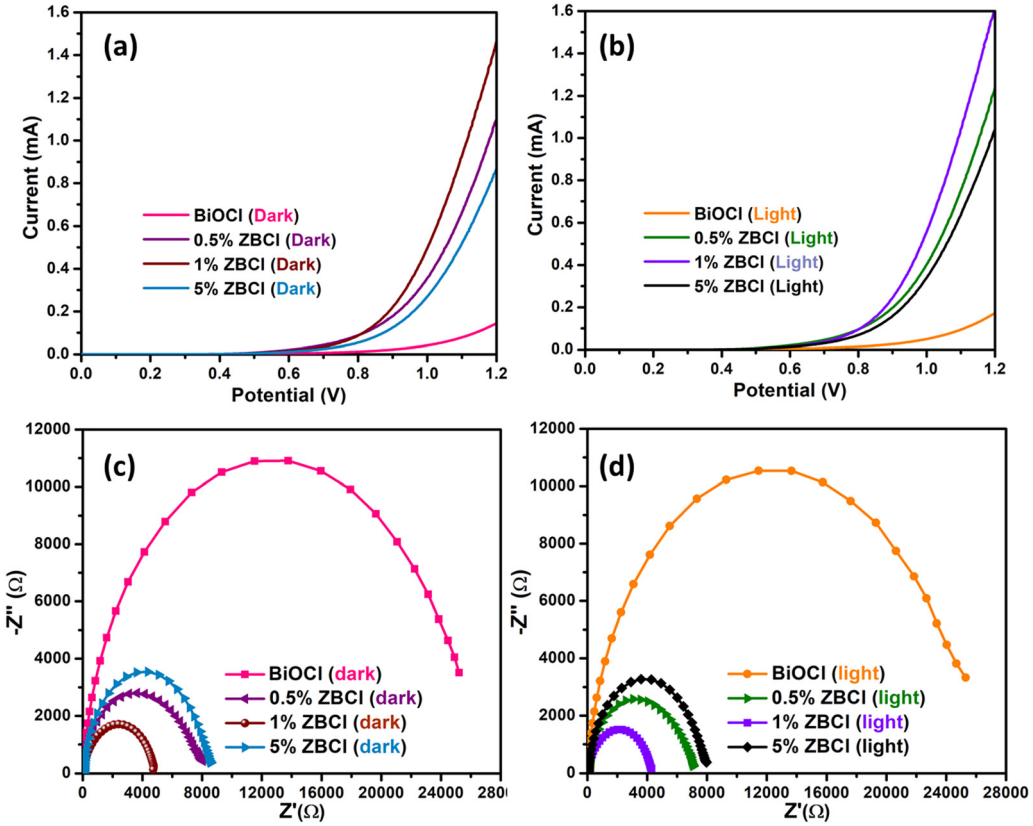

Fig. 7 (a) and (b) LSV and (c) and (d) Nyquist plot of BiOCl, 0.5% ZBCl, 1% ZBCl, and 5% ZBCl in the dark and under visible light irradiation.

and under visible light irradiation. Generally, the response under visible light irradiation should have higher current than in dark condition. Fig. 7(a) shows the current response under dark condition, in which 1% ZBCl (1.47 mA) exhibits a greater response of current than 0.5% ZBCl (1.12 mA), 5% ZBCl (0.88 mA), and BiOCl (0.14 mA). Fig. 7(b) displays the photocurrent response recorded under visible light irradiation. It was observed that 1% ZBCl exhibits a greater photocurrent response of 1.60 mA than 0.5% ZBCl (1.25 mA), 5% ZBCl (1.05 mA), and BiOCl (0.19 mA). When compared to BiOCl, the photocurrent of ZBCl steadily increases, indicating that doping with Zr could significantly increase photoconversion efficiency. The improvement in photocurrent also demonstrates the increase in photogenerated electron–hole pair separation and the rate at which photoinduced carriers are transported.[60] Based on the results, it can be deduced that 1% ZBCl have the highest current response both in the dark and under visible light irradiation. Moreover, the current response performed under visible light irradiation has better response than in dark. Hence, this indicated that 1% ZBCl possessed better electron–hole separation and can be excited easily by visible light.

EIS was used to further investigate the photoactivity of the prepared photoelectrodes in the dark and under visible light irradiation. Typically, the light response should have lower arc radius than dark response. The main factor of photocatalytic activity is the efficiency of interface charge separation of the photogenerated electrons and holes. The EIS Nyquist plots can be used to analyze the interface charge separation effectiveness.[60,61] In Fig. 7(c) and (d), the impedance arc radius of ZBCl is smaller than BiOCl with increasing doping dosage. In the case of in the (c) dark and (d) under visible light irradiation, the 1% ZBCl had the smallest radius arc followed by 0.5% ZBCl, 5% ZBCl, and BiOCl. This finding is consistent with the photocatalytic performance, where 1% ZBCl is the best. Smaller arc radius indicates greater charge transfer efficiency. This suggests that the 1% ZBCl photocatalysts have lower resistance than that of BiOCl, 0.5% ZBCl, and 5% ZBCl, which can accelerate the interfacial charge-transfer process.[62] Hence, EIS confirms that the 1% ZBCl is an effective material for photoelectrodes.[61]

6. Conclusion

This study reported a one-step facile method to prepare a visible light active Zr-doped BiOCl under ambient conditions. The XRD result confirmed tetragonal phases were obtained for BiOCl and 0.5%, 1%, and 5% ZBCl. The average crystallite sizes were between 23–34 nm. The TEM analysis showed BiOCl and ZBCl samples have irregular nanoplates with average thickness between 80–100 nm. Among the ZBCl samples, 1% ZBCl has the highest photocatalytic activity under visible light irradiation. The 1% ZBCl was able to degrade 97.7% of RhB dye within 60 min. Furthermore, 1% ZBCl also showed enhanced responses

in photoelectrochemical activities. Therefore, this study suggests that ZBCl can be potentially used as a visible light active photocatalyst and photoelectrode material.

Author contributions

Asyiqin Zulkiflee: methodology, investigation, data curation, writing – original draft. Mohammad Mansoob Khan: supervision, conceptualization, funding acquisition, writing – review & editing. Mohd Yusuf Khan: formal analysis, writing – review & editing. Abuzar Khan: formal analysis, writing – review & editing. Chennampilly Ummer: formal analysis. Mohammad Hilni Harunsani: supervision, conceptualization, funding acquisition, writing – review & editing.

Conflicts of interest

The authors declared that they have no known interests or personal relationships that could have appeared to influence the work reported in this paper.

Acknowledgements

This research was funded by Universiti Brunei Darussalam through grant FIC block grant UBD/RSCH/1.4/FICBF(b)/2021/035.

References

1 L. Ye, Y. Su, X. Jin, H. Xie and C. Zhang, *Environ. Sci. Nano*, 2014, **1**, 90.
2 I. K. Konstantinou and T. A. Albanis, *Appl. Catal., B*, 2004, **49**, 1–14.
3 H. Chen, C. E. Nanayakkara and V. H. Grassian, *Chem. Rev.*, 2012, **112**, 5919–5948.
4 X. Chen, S. Shen, L. Guo and S. S. Mao, *Chem. Rev.*, 2010, **110**, 6503–6570.
5 A. Kubacka, M. Fernández-García and G. Colón, *Chem. Rev.*, 2012, **112**, 1555–1614.
6 T. Liu, L. Wang, X. Lu, J. Fan, X. Cai, B. Gao, R. Miao, J. Wang and Y. Lv, *RSC Adv.*, 2017, **7**, 12292–12300.
7 M. Ismail, Z. Wu, L. Zhang, J. Ma, Y. Jia, Y. Hu and Y. Wang, *Chemosphere*, 2019, **228**, 212–218.
8 K. E. Ahmed, D. H. Kuo and L. W. Duresa, *J. Ind. Eng. Chem.*, 2020, **83**, 200–207.
9 V. Katheresan, J. Kansedo and S. Y. Lau, *J. Environ. Chem. Eng.*, 2018, **6**, 4676–4697.
10 P. Bansal, D. Singh and D. Sud, *Sep. Purif. Technol.*, 2010, **72**, 357–365.
11 Y. Li, Y. L. Li, B. Sa and R. Ahuja, *Catal. Sci. Technol.*, 2017, **7**, 545–559.
12 A. G. Akerdi and S. H. Bahrami, *J. Environ. Chem. Eng.*, 2019, **7**, 103283.
13 C. Zhou, C. Lai, C. Zhang, G. Zeng, D. Huang, M. Cheng, L. Hu, W. Xiong, M. Chen, J. Wang, Y. Yang and L. Jiang, *Appl. Catal., B*, 2018, **238**, 6–18.
14 J. Low, J. Yu, M. Jaroniec, S. Wageh and A. A. Al-Ghamdi, *Adv. Mater.*, 2017, **29**, 1601694.
15 H. Sudrajat, S. Babel, A. T. Ta and T. K. Nguyen, *J. Phys. Chem. Solids*, 2020, **144**, 109517.
16 P. Hegedűs, E. Szabó-Bárdos, O. Horváth, P. Szabó and K. Horváth, *Catal. Today*, 2017, **284**, 179–186.
17 Z. Li, K. H. Ng, S. Xu, Y. Zhang, Y. Lei, J. Huang and Y. Lai, *Chemosphere*, 2022, **307**, 135758.
18 W. Cui, H. Bai, J. Shang, F. Wang, D. Xu, J. Ding, W. Fan and W. Shi, *Electrochim. Acta*, 2020, **349**, 136383.
19 Y. Zhang, Y. Lei, T. Zhu, Z. Li, S. Xu, J. Huang, X. Li, W. Cai, Y. Lai and X. Bao, *Chin. J. Chem. Eng.*, 2022, **41**, 403–411.
20 Y. Zheng, X. Hu, C. Wu, M. Chen, Q. Chen, Y. Wang, S. Hu, J. Xiang, Q. Liu, X. Zhang and P. Yang, *J. Phys. Chem. Solids*, 2019, **135**, 109119.
21 P. Gao, Y. Yang, Z. Yin, F. Kang, W. Fan, J. Sheng, L. Feng, Y. Liu, Z. Du and L. Zhang, *J. Hazard. Mater.*, 2021, **412**, 125186.
22 D. Kato, K. Hongo, R. Maezono, M. Higashi, H. Kunioku, M. Yabuuchi, H. Suzuki, H. Okajima, C. Zhong, K. Nakano, R. Abe and H. Kageyama, *J. Am. Chem. Soc.*, 2017, **139**, 18725–18731.
23 S. Ning, X. Shi, H. Zhang, H. Lin, Z. Zhang, J. Long, Y. Li and X. Wang, *Sol. RRL*, 2019, **3**, 1900059.
24 D. H. Wang, G. Q. Gao, Y. W. Zhang, L. S. Zhou, A. W. Xu and W. Chen, *Nanoscale*, 2012, **4**, 7780–7785.
25 K. Wangkawong, S. Phanichphant, D. Tantraviwat and B. Inceesungvorn, *J. Taiwan Inst. Chem. Eng.*, 2020, **108**, 55–63.
26 H. Deng, J. Wang, Q. Peng, X. Wang and Y. Li, *Chem. – Eur. J.*, 2005, **11**, 6519–6524.
27 J. Henle, P. Simon, A. Frenzel, S. Scholz and S. Kaskel, *Chem. Mater.*, 2007, **19**, 366–373.
28 J. Hu, W. Fan, W. Ye, C. Huang and X. Qiu, *Appl. Catal., B*, 2014, **158–159**, 182–189.
29 J. Song, Q. Fan, W. Zhu, R. Wang and Z. Dong, *Mater. Lett.*, 2016, **165**, 14–18.
30 P. Persson, M. J. Lundqvist, R. Ernstorfer, W. A. Goddard and F. Willig, *J. Chem. Theory Comput.*, 2006, **2**, 441–451.
31 W. Liu, Y. Shang, A. Zhu, P. Tan, Y. Liu, L. Qiao, D. Chu, X. Xiong and J. Pan, *J. Mater. Chem. A*, 2017, **5**, 12542–12549.
32 S. Liang, D. Zhang, X. Yao, R. Han, Q. Zhang, C. Jin, X. Pu and Y. Geng, *Sep. Purif. Technol.*, 2020, **238**, 116450.
33 X. Wang, X. Liu, G. Liu, C. Zhang, G. Liu, S. Xu, P. Cui and D. Li, *Catal. Commun.*, 2019, **130**, 105769.
34 X. Gao, W. Peng, G. Tang, Q. Guo and Y. Luo, *J. Alloys Compd.*, 2018, **757**, 455–465.
35 D. Cui, L. Wang, K. Xu, L. Ren, L. Weng, Y. Yu, Y. Du and W. Hao, *J. Mater. Chem. A*, 2018, **6**, 2193–2199.
36 F. Mokhtari and N. Tahmasebi, *J. Phys. Chem. Solids*, 2021, **149**, 109804.
37 A. Zulkiflee, M. M. Khan and M. H. Harunsani, *Mater. Sci. Semicond. Process.*, 2023, **163**, 107547.

38 K. Xu, X. Fu and Z. Peng, *Mater. Res. Bull.*, 2018, **98**, 103–110.
39 C. Y. Wang, Y. J. Zhang, W. K. Wang, D. N. Pei, G. X. Huang, J. J. Chen, X. Zhang and H. Q. Yu, *Appl. Catal., B*, 2018, **221**, 320–328.
40 B. Pare, B. Sarwan and S. B. Jonnalagadda, *Appl. Surf. Sci.*, 2011, **258**, 247–253.
41 Y. I. Choi, K. H. Jeon, H. S. Kim, J. H. Lee, S. J. Park, J. E. Roh, M. M. Khan and Y. Sohn, *Sep. Purif. Technol.*, 2016, **160**, 28–42.
42 F. Xie, X. Mao, C. Fan and Y. Wang, *Mater. Sci. Semicond. Process.*, 2014, **27**, 380–389.
43 J. Xie, Y. Cao, D. Jia, H. Qin and Z. Liang, *Catal. Commun.*, 2015, **69**, 34–38.
44 S. S. Imam, R. Adnan and N. H. M. Kaus, *Res. Chem. Intermed.*, 2018, **44**, 5357–5376.
45 W. Tang, Y. Zhang, H. Guo and Y. Liu, *RSC Adv.*, 2019, **9**, 14060–14071.
46 J. Jiang, K. Zhao, X. Xiao and L. Zhang, *J. Am. Chem. Soc.*, 2012, **134**, 4473–4476.
47 J. Ma, X. Liu, J. Lian, X. Duan and W. Zheng, *Cryst. Growth Des.*, 2010, **10**, 2522–2527.
48 J. Yang, T. Xie, C. Liu and L. Xu, *Nanomaterials*, 2018, **8**, 697.
49 J. Di, J. Xia, S. Yin, H. Xu, L. Xu, Y. Xu, M. He and H. Li, *RSC Adv.*, 2014, **4**, 14281.
50 S. Kang, R. C. Pawar and C. S. Lee, *J. Exp. Nanosci.*, 2016, **11**, 853–871.
51 W. J. Kim, D. Pradhan, B.-K. Min and Y. Sohn, *Appl. Catal., B*, 2014, **147**, 711–725.
52 J. Xia, L. Xu, J. Zhang, S. Yin, H. Li, H. Xu and J. Di, *CrystEngComm*, 2013, **15**, 10132–10141.
53 J. Liqiang, Q. Yichun, W. Baiqi, L. Shudan, J. Baojiang, Y. Libin, F. Wei, F. Honggang and S. Jiazhong, *Sol. Energy Mater. Sol. Cells*, 2006, **90**, 1773–1787.
54 R. Mani, K. Vivekanandan and K. Vallalperuman, *J. Mater. Sci.: Mater. Electron.*, 2017, **28**, 4396–4402.
55 R. Mani, K. Vivekanandan and N. P. Subiramaniyam, *J. Mater. Sci.: Mater. Electron.*, 2017, **28**, 13846–13852.
56 J. Liqiang, S. Xiaojun, X. Baifu, W. Baiqi, C. Weimin and F. Honggang, *J. Solid State Chem.*, 2004, **177**, 3375–3382.
57 Y. Mi, L. Wen, Z. Wang, D. Cao, R. Xu, Y. Fang, Y. Zhou and Y. Lei, *Nano Energy*, 2016, **30**, 109–117.
58 M. Thommes, K. Kaneko, A. V. Neimark, J. P. Olivier, F. Rodriguez-Reinoso, J. Rouquerol and K. S. W. Sing, *Pure Appl. Chem.*, 2015, **87**, 1051–1069.
59 N. Tahmasebi, S. Mirzavand, A. Hakimyfard and S. Barzegar, *Adv. Powder Technol.*, 2019, **30**, 257–265.
60 M. M. Khan, S. A. Ansari, D. Pradhan, M. O. Ansari, D. H. Han, J. Lee and M. H. Cho, *J. Mater. Chem. A*, 2014, **2**, 637–644.
61 S. A. Ansari, M. M. Khan, M. O. Ansari, J. Lee and M. H. Cho, *J. Phys. Chem. C*, 2013, **117**, 27023–27030.
62 Y. Zheng, T. Gao, S. Chen, C. T. J. Ferguson, K. A. I. Zhang, F. Fang, Y. Shen, N. A. Khan, L. Wang and L. Ye, *Compos. Commun.*, 2022, **36**, 101390.